J. Phys. B: At. Mol. Opt. Phys. **40** (2007) 3453–3466 doi:10.1088/0953-4075/40/17/012

Spin polarization of the Ar* $2p_{1/2}^{-1}$ 4s and $2p_{1/2}^{-1}$ 3d resonant Auger decay

G Turri[1,2,6], B Lohmann[3,4], B Langer[5], G Snell[1,2], U Becker[4] and N Berrah[1]

[1] Department of Physics, Western Michigan University, Kalamazoo, MI 49008, USA
[2] Advanced Light Source, Lawrence Berkeley National Laboratory, Berkeley, CA 94720, USA
[3] Institut für Theoretische Physik, Westfälische Wilhelms-Universität Münster, Wilhelm-Klemm-Strasse 9, D-48149 Münster, Germany
[4] Fritz-Haber-Institut der Max-Planck-Gesellschaft, Faradayweg 4-6, D-14195 Berlin/Dahlem, Germany
[5] Max-Born-Institut für Nichtlineare Optik und Kurzzeitspektroskopie, Max-Born-Strasse 2A, D-12489 Berlin, Germany

Received 10 April 2007, in final form 25 July 2007
Published 28 August 2007
Online at stacks.iop.org/JPhysB/40/3453

Abstract

The spin-resolved Auger decay of the Ar $2p_{1/2}^{-1}$ 3d state was measured at moderate energy resolution and compared with the decay of the $2p_{1/2}^{-1}$ 4s. The former shows a lower transferred spin polarization and a similar, if not higher, dynamical spin polarization, supporting the statement that a fully resolved spectrum is not a necessary condition for observing dynamical spin polarization. An interpretation of the spin polarization as configuration interaction induced effect in the final ionic state leads to partial agreement with our relativistic distorted wave calculation utilizing a 36 configuration state function basis set. Comparison of the experimental and numerical results leads to ambiguities for at least one Auger line. A hypothetical, qualitative interpretation is discussed.

(Some figures in this article are in colour only in the electronic version)

1. Introduction

A variety of experimental and theoretical investigations have been concerned with electron emission of either normal or resonant Auger decay, where, under certain conditions, the Auger electrons can be spin polarized [1–10]. As for the electrons emitted by direct photoionization, the spin polarization is caused by the spin–orbit interaction either in the atom or in the continuum, and the two different mechanisms of transferred spin polarization (TSP) [1–10] and dynamic spin polarization (DSP) [6, 7, 10] can be distinguished. TSP occurs because of the intrinsic polarization of the incoming photon, which generates an asymmetric sublevel population in the atom which is eventually transferred to the emitted Auger electrons, while

[6] Present address: CREOL, The College of Optics and Photonics, University of Central Florida, Orlando, FL, USA.

 © 2007 IOP Publishing Ltd Printed in the UK

the DSP is generated dynamically, i.e. by relativistic or spin–orbit effects during the Auger emission, and therefore requires no intrinsic spin polarization. In general, DSP in atoms vanishes when measurements integrate the emission angle of the electrons, whereas TSP can still be non-zero. Also, there may be particular reasons for small or vanishing DSP in an atom showing high TSP. As has been discussed in [8], resonant Auger decay from 2p excited argon atoms is a showcase for large TSP but vanishing DSP. A large TSP can be expected, and has been measured, for the $2p^{-1}$ 4s state and might be understood from the close similarity of the Auger emission with d shell photoionization. As in that case, the Auger electron can be emitted as a p-wave only, due to the suppression of the f-wave by the centrifugal barrier, resulting in large TSP [4, 8]. A low DSP results from the fact that electrons are emitted with partial waves with equal orbital angular momentum, thus resulting in small phase difference in the continuum due to relativistic effects only. In general, it is also believed that DSP should vanish when the fine structure of the LS multiplet is not resolved. In our previous work [8], we showed that the last statement is not necessarily true, and that some small DSP can still be observed also in the case of partially unresolved fine structure, due to strong configuration interaction in the final ionic state.

In the present work, we are extending our former investigation to the Auger decay of the $2p^{-1}$ 3d excited state in argon and report on a combined experimental and theoretical analysis and interpretation of both TSP and DSP in one spectrum. As compared to the $2p_{1/2}^{-1}$ 4s state that mainly decays to final $3p^4nl$ states of binding energy between 32 and 38 eV, the most intense transitions from the $2p_{1/2}^{-1}$ 3d are to states between 37 and 41 eV binding energy. Also, some states in the 32–38 eV range can be more efficiently populated from the $2p_{1/2}^{-1}$ 3d than from the $2p_{1/2}^{-1}$ 4s excited state [11]. On a fundamental level, the mechanism of the Auger process is different for the two states: whereas the decay of the $2p^{-1}$ 4s can be well explained with a spectator model, shake-up processes dominate the decay of the $2p^{-1}$ 3d [12–16]. The latter behaviour has been discussed first by Aksela *et al* [13] and then by Meyer *et al* [14, 15] in terms of the partial collapse of the 3d wavefunction between the initial and the final state. Later, Langer *et al* [16] further investigated the effects of the collapsed 3d orbital on the mixing of the core and hole states, showing how even a spectator model modified to account for shake-up processes fails to describe the angular distribution of the $2p_{1/2}^{-1}$ 3d Auger peaks.

The experimental results will be compared with calculations based on the relativistic distorted wave approximation technique described in our previous paper [8], utilizing configuration interaction of the configuration state function basis set for the initial, intermediate and final states opportunely modified for the $2p^{-1}$ 3d case. An interesting hypothesis will be discussed for a line having a large DSP which, from the present investigation, we are not able to fully explain in terms of multi-step two-body interaction. In addition, our previous investigation of the $2p^{-1}$ 4s decay will be extended to a broader energy range with new measurements.

The paper is organized as follows. In the next section the theoretical background will be shortly reviewed, while in section 3 the experimental details and set-up are considered. The numerical methods will be discussed in section 4. Our results are discussed in section 5, and a short conclusion is given in the last section.

2. Theory

Applying the experimentally well-observed two-step model, e.g. see [17], we are considering the angle- and spin-resolved, resonantly excited Auger decay of argon, where the primary

excitation is either to the $4s_{1/2}$ or $3d_{3/2}$ Rydberg levels

$$\gamma + \mathrm{Ar}(^1\mathrm{S}_0) \longrightarrow \begin{cases} \mathrm{Ar}^*\left(2p_{1/2}^{-1}, 4s_{1/2}\right)_{J=1}, \\ \mathrm{Ar}^*\left(2p_{1/2}^{-1}, 3d_{3/2}\right)_{J=1}, \end{cases}$$
$$\longrightarrow \mathrm{Ar}^{+*}\left(3p_{1/2,3/2}^{-2}, 4s_{1/2} + 3d_{3/2,5/2}\right) L_{J=1/2,\ldots,9/2}^{2S+1=2,4} + \mathrm{e}_{\mathrm{Auger}}. \tag{1}$$

For the independent treatment of the two decay processes we refer to the discussion in section 4.

The general equations for the angular distribution and the Cartesian components of the spin polarization vector have been derived by Kleiman *et al* [18] in the helicity frame of the emitted Auger electrons with the axis of Auger emission as quantization axis. For such a geometry, both the angular distribution and the spin polarization vector can be related to an arbitrary chosen coordinate frame, e.g. the laboratory frame, via two angles θ and ϕ defined with respect to the quantization axis. The two-step model allows for a factorization of the angular distribution and spin polarization parameters. In addition, the dipole approximation restricts the number of parameters, i.e. only parameters with rank $K \leqslant 2$ contribute. Thus, we obtain the angular distribution as

$$I(\theta, \phi)^\gamma = \frac{I_0}{4\pi}\left\{1 + \alpha_2\left(\mathcal{A}_{20} P_2(\cos\theta) + \sqrt{\frac{3}{2}}[\mathrm{Re}\,\mathcal{A}_{22}\cos 2\phi - \mathrm{Im}\,\mathcal{A}_{22}\sin 2\phi]\sin^2\theta\right)\right\}, \tag{2}$$

where I_0 denotes the total intensity and $P_2(\cos\theta)$ is the second Legendre polynomial.

The Cartesian components of the spin polarization vector can be expressed as

$$p_x(\theta, \phi)^\gamma = \frac{1}{N^\Gamma}(\xi_1 \mathcal{A}_{10} + \sqrt{6}\xi_2\,[\mathrm{Re}\,\mathcal{A}_{22}\sin 2\phi + \mathrm{Im}\,\mathcal{A}_{22}\cos 2\phi])\sin\theta, \tag{3}$$

$$p_y(\theta, \phi)^\gamma = \frac{-3}{2N^\Gamma}\xi_2\left(\mathcal{A}_{20} - \sqrt{\frac{2}{3}}\,[\mathrm{Re}\,\mathcal{A}_{22}\cos 2\phi - \mathrm{Im}\,\mathcal{A}_{22}\sin 2\phi]\right)\sin 2\theta, \tag{4}$$

and

$$p_z(\theta, \phi)^\gamma = \frac{1}{N^\Gamma}\delta_1\,\mathcal{A}_{10}\cos\theta, \tag{5}$$

where we introduced the abbreviation $N^\Gamma = 4\pi\, I(\theta, \phi)^\gamma / I_0$. Note that the numerator of (5) remains independent of the azimuth ϕ. This can be explained by the fact that, irrespective of the specific choice of the X- and Y-axes of the laboratory frame, the z-axis of the helicity frame is always contained in the reaction plane.

The dynamics of the photoexcitation into the intermediate excited Ar* state is described by a set of state multipoles A_{KQ}. Particularly, A_{10} and A_{20} are known as orientation and alignment parameters, respectively. For our case of a primary photoexcitation they become constant numbers, and take their maximum values for specific geometries, e.g. see [19]. The Auger decay dynamics is described by the (intrinsic) angular distribution parameter α_2 and spin polarization parameters δ_1 and ξ_1, referring to the TSP and ξ_2 related to the DSP, respectively. They are combinations of the matrix elements and phases of the second step Auger decay only.

Inspecting equations (2)–(5), we find that only (3) allows for observing either the TSP or the DSP within the same experimental set-up (see section 3). Here, the first depends on the orientation parameter A_{10}, while the latter depends on the real and imaginary components A_{22} of the alignment tensor.

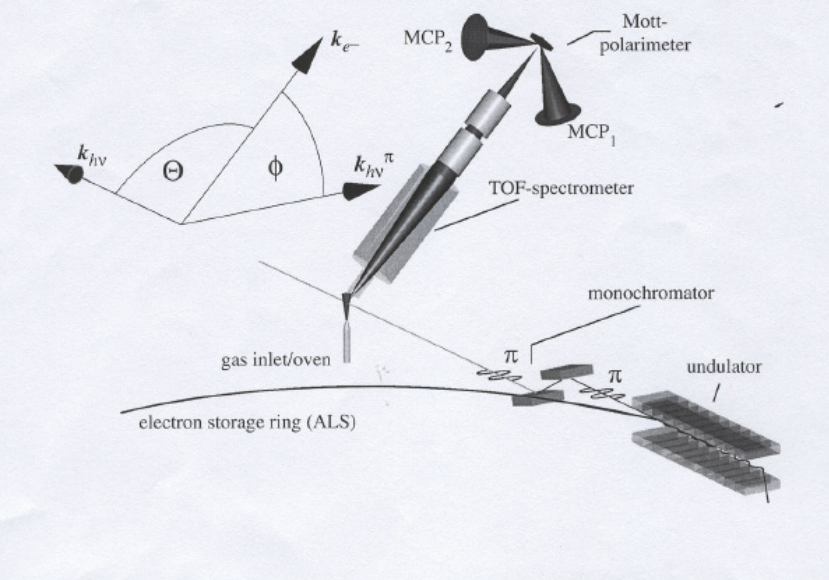

Figure 1. Experimental set-up with undulator beamline, TOF electron analyser and Mott detector [32].

3. Experimental set-up

Measurements were performed at the beamline 4.0.2 at the advanced light source (ALS) at Lawrence Berkeley National Laboratory in Berkeley, CA. The elliptically polarized undulator (EPU) was set to deliver either linearly or circularly polarized light (polarization 100% in both cases), with energy of 246.4 eV or 249.0 eV to excite the $2p_{1/2}^{-1}$ 4s and $2p_{1/2}^{-1}$ 3d resonances, respectively. The experimental geometry is illustrated in figure 1. Auger electrons were collected in a plane perpendicular to the photon propagation direction and at 45° with respect to the plane of the storage ring. Their kinetic energy was measured by time-of-flight (TOF) detectors [20]. A Mott detector of the Rice type [21, 22], operated at 25 kV, $S_{\mathrm{eff}} = 0.13 \pm 0.02$, mounted after the drift tube of the TOF detector, measured the spin polarization along the photon propagation axis. Geometrical asymmetries of the apparatus were accounted for, by the standard technique of reversing the helicity of the photons when using circularly polarized light and rotating by 90° the polarization of linearly polarized light. Within the described geometry, the equations for the TSP and DSP can be derived from (3) and take the simple forms [20 and references therein]

$$\mathrm{P}_{\mathrm{trans}}(\theta) = \frac{2\sqrt{3}\xi_1}{2\sqrt{2} - \alpha_2}, \tag{6}$$

$$\mathrm{P}_{\mathrm{dyn}}(\theta,\phi) = \frac{6\xi_2}{2\sqrt{2} - \alpha_2}. \tag{7}$$

Note that the azimuthal angle ϕ becomes redundant for the TSP. The transferred and dynamic electron spin polarizations, corresponding to $P_{\mathrm{trans}}(\theta = 90^\circ)$ and $P_{\mathrm{dyn}}(\theta = 90^\circ, \phi = 135^\circ)$, respectively, can be calculated from the four measured spin-up and spin-down intensities I_1^+,

I_1^-, I_2^+ and I_2^- as follows:

$$P_{\mathrm{trans,dyn}}(\theta,\phi) = \frac{1}{S_{\mathrm{eff}}} \frac{\sqrt{I_1^+ I_2^-} - \sqrt{I_1^- I_2^+}}{\sqrt{I_1^+ I_2^-} + \sqrt{I_1^- I_2^+}}. \tag{8}$$

The experimental angle $\Phi = 45^\circ$ for collecting the electrons with respect to the storage ring plane (see figure 1) refers to $\phi = 135^\circ$ in our chosen coordinate frame.

4. Numerical methods

In order to obtain the numerical data from equations (6) and (7), we employed a relativistic distorted wave approximation (RDWA), which has been briefly outlined in [8]. Here, the bound state wavefunctions of the excited intermediate and the ionized final atomic states are constructed using the multiconfigurational Dirac–Fock (MCDF) computer code of Grant *et al* [23]. Intermediate coupling has been taken into account obtaining the mixing coefficients by applying the average level calculation mode [23]. The calculation of the Auger transition matrix elements has been performed applying a relaxed orbital method [24, 25], utilizing the ANISO program package [26], calculating the bound electron wavefunctions of the intermediate state in the field of the excited atom, whereas obtaining the bound electron wavefunctions of the final state in the field of the singly ionized atom.The atomic state function (ASF) of the intermediate excited and the singly ionized final state has been constructed as linear combinations of configuration state functions (CSF):

$$|\psi_\alpha(PJM)\rangle = \sum_{r=1}^{n_c} c_r(\alpha)|\gamma_r PJM\rangle. \tag{9}$$

The configuration states $|\gamma_r PJM\rangle$ are constructed from antisymmetrized products of Dirac orbitals which are eigenstates of the total (one-electron) angular momentum and parity. The label γ_r distinguish the occupation of the different subshells and angular coupling schemes (see [27] for further details). n_c is the number of CSF included in the expansion and $c_r(\alpha)$, $r = 1, \ldots, n_c$, are the configuration mixing coefficients for the state α.

We generated the intermediate excited state as a linear combination of the five possible jj-coupled $\mathrm{Ar}^*\left(2p_{1/2,3/2}^{-1}\,4s_{1/2}\right)_{J=1}$ and $\mathrm{Ar}^*\left(2p_{1/2,3/2}^{-1}\,3d_{3/2,5/2}\right)_{J=1}$ CSF. Our calculation yields the $\mathrm{Ar}^*\left(2p_{3/2}^{-1}\,4s_{1/2}\right)_{J=1}$ and $\mathrm{Ar}^*\left(2p_{1/2}^{-1}\,4s_{1/2}\right)_{J=1}$ as well as the $\mathrm{Ar}^*\left(2p_{1/2}^{-1}\,3d_{3/2}\right)_{J=1}$ ASF as almost pure states. This allows for separately discussing our $L_2M_{2,3}M_{2,3}$ Auger decay data obtained from the $2p_{1/2}^{-1} \rightarrow 4s$ and $2p_{1/2}^{-1} \rightarrow 3d$ excitation processes, respectively. However, strong intermediate coupling has been found between the $\mathrm{Ar}^*\left(2p_{3/2}^{-1}\,3d_{3/2}\right)_{J=1}$ and the $\mathrm{Ar}^*\left(2p_{3/2}^{-1}\,3d_{5/2}\right)_{J=1}$ ASF.

A configuration interaction (CI) calculation has been performed for the final ionic state, i.e., all possible linear combinations of the $\mathrm{Ar}^+\left(3p_{1/2,3/2}^{-2}\,4s_{1/2}\right)$ and $\mathrm{Ar}^+\left(3p_{1/2,3/2}^{-2}\,3d_{3/2,5/2}\right)$ jj-coupled states, forming a basis set of 36 CSF, have been included in generating the final state ASF (36 CSF-CI).[7]

We note that the collapse of the 3d orbital has no effect on the resonant Auger decay of the exited 2p states, as it causes a strong satellite line in the inner valence region of Ar only

[7] Recently, the $\mathrm{Ar}(3p^4 nl)$ photoelectron satellites have been measured varying the photoexcitation energy across the $\mathrm{Ar}^*(2p_{1/2}^{-1}\,4s_{1/2})_{J=1}$ and $\mathrm{Ar}^*(2p_{3/2}^{-1}\,3d_{3/2,5/2})_{J=1}$ resonances [28], finding correlation patterns between the initial and the resulting final fine structure states as a function of the photoelectron energy. While our calculation confirms strong correlations for the final state configuration interaction (CI), we obtained the initial states of the Auger transition as almost pure.

[29]. Eventually, we are evaluating the continuum wavefunction of the Auger electron by solving the Dirac equation with an intermediate coupling potential where electron exchange with the continuum has been taken into account. The intermediate coupling potential is constructed from the mixed CSF of the final ionic state. Thereby we take into account that the ejected electron moves within the field of the residual ion. Employing the ANISO package [26], the Auger transition matrix elements are obtained for calculating the relevant angular anisotropy and spin polarization parameters, respectively. Note that both are not functions of the transition matrix elements only but explicitly depend on the scattering phases. More detailed information may be found in [24, 25].

5. Results

Our numerical data for the relative intensities, angular distribution and spin polarization parameters which have been obtained from our 36 CSF-CI are shown in table 1 for the $\mathrm{Ar}^*\left(2\mathrm{p}_{1/2}^{-1} \rightarrow 4\mathrm{s}_{1/2}\right)_{J=1}$ and in table 2 for the $\mathrm{Ar}^*\left(2\mathrm{p}_{1/2}^{-1} \rightarrow 3\mathrm{d}_{3/2}\right)_{J=1}$ $\mathrm{L_2M_{2,3}M_{2,3}}$ resonant Auger decay. The jj-coupling notation, which is the natural scheme for a relativistic approach (e.g. see [27]), has been used for identifying the main contribution of the relevant final states. Inspecting both tables, we find the high J part for certain multiplets, e.g. line 6 of table 1, or line 10 of table 2, suppressed due to internal J-dependent selection rules [8]. This has been indicated by an en dash in the tables. Particularly, Auger transitions to the $J_\mathrm{f} = 7/2$ and $9/2$ final states are suppressed for the $\mathrm{Ar}^*\left(2\mathrm{p}_{1/2}^{-1}\,4\mathrm{s}_{1/2}\right)_{J=1}$ and to the $J_\mathrm{f} = 9/2$ final fine structure states for the $\mathrm{Ar}^*\left(2\mathrm{p}_{1/2}^{-1}\,3\mathrm{d}_{3/2}\right)_{J=1}$ intermediate excited states, respectively. As has been discussed in [8], this results in surviving of the low J fine structure components of a multiplet only, with no partner for polarization cancellation of the DSP.

From the data of tables 1 and 2, the relevant spin-up and spin-down intensities have been obtained by performing a weighted sum over the fine structure states, and where appropriate summing over two or more unresolved lines, in order to allow for a comparison with the experimental low resolution line spectra. Note that the numerical spectrum usually needs to be shifted by an energy offset and re-normalized to the experimental total intensities. Since our 36 CSF-CI does not cover the full energy range of the observed spectrum, a comparison with the experimental data for the DSP and TSP has been possible for lines 1–7 of the measured Auger spectra only. The assignment between the line and peak numbers may be found in table 4. The numerical results of lines 1–9 for the $\mathrm{Ar}^*\left(2\mathrm{p}_{1/2}^{-1} \rightarrow 3\mathrm{d}_{3/2}\right)_{J=1}$ $\mathrm{L_2M_{2,3}M_{2,3}}$ spectrum are positioned outside the observed energy range. However, they have been used for our previous spin-resolved analysis of the unresolved peak structure of the $\mathrm{Ar}^*\left(2\mathrm{p}_{1/2,3/2}^{-1} \rightarrow 4\mathrm{s}_{1/2}\right)_{J=1}$ $\mathrm{L_2M_{2,3}M_{2,3}}$ spectrum [8] and have been included in the calculation for a consistent comparison of the data.

In figure 2, the spin-unresolved spectrum (average of spin-up and spin-down spectra) of the $2\mathrm{p}_{1/2}^{-1}$ 3d Auger decay measured with circularly polarized light is displayed. It consists of some 15 peaks, where every peak is a manifold of many overlapping components, corresponding to the transitions to the different final states of the singly ionized argon atom. The correct assignment of the peaks is not straightforward, especially for time-of-flight measurements, where small errors in the kinetic energy scale may occur due to the time to energy conversion. The number of the Ar^+ states, their binding energy and the relative intensities of the Auger transitions from the Ar $2\mathrm{p}_{1/2}^{-1}$ 3d state are known from [11, 16, 30, 31]. The angular distribution has also been measured for many transitions [12, 16, 31] whereas the spin polarization has not been measured up to now. From the values of [11, 12, 16], we were able to identify the components of all the peaks, and we report them in table 3: very weak transitions have

Table 1. The energies, relative intensities, angular distribution and spin polarization parameters for the $Ar^*(2p_{1/2}^{-1}\,4s_{1/2})_{J=1}\,L_2M_{2,3}M_{2,3}$ Auger transitions. A zero for the ξ_2 parameter denotes that the Auger emission is via one partial wave only. –: suppressed. (a) The leading jj-coupled configuration state function has been used to identify the state. (b) Percentage of leading CSF (see the text for details).

	$Ar^*(4s_{1/2})L_2M_{2,3}M_{2,3}$							
	Final states		Energy	Intensity	Angular and spin polarization parameters			
No	(a)	(b) (%)	(eV)	I_0	σ_2	δ_1	ξ_1	ξ_2
1	$\|([3\bar{p}^2 3p^2]_2 4s^1)5/2\rangle$	69.6	215.942	3.506	−0.135	−0.270	−0.478	−0.0040
2	$\|([3\bar{p}^1 3p^3]_1 3\bar{d}^1)1/2\rangle$	71.6	215.843	2.929	−0.628	0.454	0.837	−0.0004
3	$\|([3\bar{p}^2 3p^2]_2 3\bar{d}^1)3/2\rangle$	28.0	215.842	0.206	0.584	0.196	0.310	−0.0121
4	$\|([3\bar{p}^1 3p^3]_1 4s^1)3/2\rangle$	54.6	215.827	6.542	0.557	0.149	0.334	0.0056
5	$\|([3\bar{p}^2 3p^2]_2 3\bar{d}^1)5/2\rangle$	32.8	215.823	0.178	−0.146	−0.225	−0.500	0.0032
6	$\|([3\bar{p}^2 3p^2]_2 3d^1)7/2\rangle$	44.0	215.791	–	–	–	–	–
7	$\|([3\bar{p}^0 3p^4]_0 4s^1)1/2\rangle$	38.1	215.762	4.549	−1.325	0.051	−0.347	0.0056
8	$\|([3\bar{p}^2 3p^2]_2 4s^1)3/2\rangle$	53.0	215.358	0.471	0.615	0.263	0.269	−0.0375
9	$\|([3\bar{p}^1 3p^3]_1 4s^1)1/2\rangle$	60.6	215.227	3.809	0.549	1.133	0.455	−0.0055
10	$\|([3\bar{p}^2 3p^2]_2 3d^1)9/2\rangle$	7.4	214.707	–	–	–	–	–
11	$\|([3\bar{p}^1 3p^3]_1 3d^1)7/2\rangle$	52.0	214.662	–	–	–	–	–
12	$\|([3\bar{p}^1 3p^3]_1 3\bar{d}^1)5/2\rangle$	52.8	214.631	1.444	−0.139	−0.254	−0.485	−0.0013
13	$\|([3\bar{p}^1 3p^3]_1 3\bar{d}^1)3/2\rangle$	40.2	214.611	2.932	0.567	0.165	0.326	−0.0007
14	$\|([3\bar{p}^2 3p^2]_2 3\bar{d}^1)1/2\rangle$	68.1	214.080	0.387	−0.171	0.718	0.853	−0.0028
15	$\|([3\bar{p}^2 3p^2]_2 3\bar{d}^1)3/2\rangle$	33.4	214.038	0.876	0.559	0.153	0.332	0.0039
16	$\|([3\bar{p}^2 3p^2]_2 3d^1)1/2\rangle$	67.0	213.995	0.122	−1.406	0.005	−0.108	0.0055
17	$\|([3\bar{p}^1 3p^3]_1 3d^1)5/2\rangle$	42.7	213.958	0.482	−0.122	−0.315	−0.454	−0.0111
18	$\|([3\bar{p}^1 3p^3]_2 3d^1)3/2\rangle$	34.8	213.873	0.411	−0.596	−0.258	−0.257	0.1779
19	$\|([3\bar{p}^1 3p^3]_2 4s^1)3/2\rangle$	40.6	213.800	13.151	0.657	0.500	0.069	−0.1218
20	$\|([3\bar{p}^1 3p^3]_2 4s^1)5/2\rangle$	57.0	213.791	20.291	−0.180	0.033	−0.613	0.0424
21	$\|([3\bar{p}^2 3p^2]_2 3d^1)7/2\rangle$	33.2	213.706	–	–	–	–	–
22	$\|([3\bar{p}^1 3p^3]_1 3d^1)5/2\rangle$	39.1	213.585	3.858	−0.167	−0.117	−0.551	0.0196
23	$\|([3\bar{p}^2 3p^2]_2 3d^1)3/2\rangle$	20.9	213.306	1.093	0.658	0.450	0.120	−0.1030
24	$\|([3\bar{p}^1 3p^3]_2 3d^1)5/2\rangle$	44.3	213.189	0.299	0.050	−0.658	−0.238	−0.0695
25	$\|([3\bar{p}^1 3p^3]_2 3\bar{d}^1)7/2\rangle$	68.1	212.903	–	–	–	–	–
26	$\|([3\bar{p}^1 3p^3]_2 3d^1)9/2\rangle$	71.4	212.843	–	–	–	–	–
27	$\|([3\bar{p}^1 3p^3]_2 3\bar{d}^1)5/2\rangle$	44.2	211.628	20.096	−0.181	0.123	−0.648	0.0536
28	$\|([3\bar{p}^1 3p^3]_2 3d^1)7/2\rangle$	71.0	211.601	–	–	–	–	–
29	$\|([3\bar{p}^1 3p^3]_2 3d^1)1/2\rangle$	31.5	211.481	1.159	0.005	0.820	−0.815	−0.0000
30	$\|([3\bar{p}^2 3p^2]_0 4s^1)1/2\rangle$	47.9	210.424	3.649	0.008	0.821	−0.814	0
31	$\|([3\bar{p}^2 3p^2]_0 3\bar{d}^1)3/2\rangle$	45.0	209.474	1.666	0.505	0.754	−0.316	−0.1976
32	$\|([3\bar{p}^0 3p^4]_0 3d^1)5/2\rangle$	27.6	209.418	0.049	0.585	−0.693	0.045	−0.1011
33	$\|([3\bar{p}^2 3p^2]_2 3d^1)3/2\rangle$	45.0	208.715	3.678	0.532	0.110	0.351	0.0187
34	$\|([3\bar{p}^1 3p^3]_2 3d^1)1/2\rangle$	52.4	208.664	0.322	−0.854	0.324	0.764	0.0009
35	$\|([3\bar{p}^2 3p^2]_0 3d^1)5/2\rangle$	40.2	207.849	1.564	−0.115	−0.338	−0.442	−0.0139
36	$\|([3\bar{p}^0 3p^4]_0 3\bar{d}^1)3/2\rangle$	39.2	207.676	0.281	0.146	0.783	−0.656	−0.1956

been neglected and only the final states that bring significant contribution to the decay of the $2p_{1/2}^{-1}$ 3d excited state are reported in column 2 of table 3. We are labelling the peaks consistently with our previous publication [8], starting from the most strongly bound one around 33.5 eV binding energy.

The identification of line 2c of the $\left(2p_{1/2}^{-1}\,3d_{3/2}\right)_{J=1}$ Auger spectrum as $^2G_{9/2}$ is not straightforward, as experimentally the fine structure splitting of the ^2G doublet of ∼3 meV is

Table 2. Same as table 1 for the $Ar^*(2p_{1/2}^{-1}\,3d_{3/2})_{J=1}\,L_2M_{2,3}M_{2,3}$ Auger transitions.

	$Ar^*(3d_{3/2})L_2M_{2,3}M_{2,3}$							
	Final states		Energy	Intensity	Angular and spin polarization parameters			
No	(a)	(b) (%)	(eV)	I_0	σ_2	δ_1	ξ_1	ξ_2
1	$\|([3\bar{p}^2 3p^2]_2 4s^1)5/2\rangle$	69.6	218.291	1.882	−0.148	−0.219	−0.503	0.0043
2	$\|([3\bar{p}^1 3p^3]_1 3\bar{d}^1)1/2\rangle$	71.6	218.191	1.697	−0.707	0.408	0.817	0
3	$\|([3\bar{p}^2 3p^2]_2 3\bar{d}^1)3/2\rangle$	28.0	218.190	1.422	0.687	−0.828	−0.066	−0.0022
4	$\|([3\bar{p}^1 3p^3]_1 4s^1)3/2\rangle$	54.6	218.175	0.208	−0.165	0.099	0.642	0.0137
5	$\|([3\bar{p}^2 3p^2]_2 3\bar{d}^1)5/2\rangle$	32.8	218.171	1.156	−0.143	−0.239	−0.493	0.0010
6	$\|([3\bar{p}^2 3p^2]_2 3d^1)7/2\rangle$	44.0	218.140	0.000	−0.202	−0.175	0.525	0
7	$\|([3\bar{p}^0 3p^4]_0 4s^1)1/2\rangle$	38.1	218.111	0.112	−0.707	0.408	0.816	0
8	$\|([3\bar{p}^2 3p^2]_2 4s^1)3/2\rangle$	53.0	217.707	3.683	0.596	0.104	0.284	−0.0049
9	$\|([3\bar{p}^1 3p^3]_1 4s^1)1/2\rangle$	60.6	217.576	0.213	−0.707	0.408	0.816	0
10	$\|([3\bar{p}^2 3p^2]_2 3d^1)9/2\rangle$	71.4	217.056	–	–	–	–	–
11	$\|([3\bar{p}^1 3p^3]_1 3d^1)7/2\rangle$	52.0	217.011	0.001	−0.202	−0.175	0.525	0
12	$\|([3\bar{p}^1 3p^3]_1 3\bar{d}^1)5/2\rangle$	52.8	216.980	5.634	−0.142	−0.241	−0.492	0.0005
13	$\|([3\bar{p}^1 3p^3]_1 3\bar{d}^1)3/2\rangle$	40.2	216.960	5.656	0.042	0.832	0.801	0.0015
14	$\|([3\bar{p}^2 3p^2]_2 3\bar{d}^1)1/2\rangle$	68.1	216.429	0.023	−0.707	0.408	0.816	0
15	$\|([3\bar{p}^2 3p^2]_2 3\bar{d}^1)3/2\rangle$	33.4	216.387	0.303	0.042	−0.500	0.362	−0.0022
16	$\|([3\bar{p}^2 3p^2]_2 3d^1)1/2\rangle$	67.0	216.344	1.561	−0.707	0.408	0.816	0
17	$\|([3\bar{p}^1 3p^3]_1 3d^1)5/2\rangle$	42.7	216.307	0.887	−0.131	−0.285	−0.470	−0.0064
18	$\|([3\bar{p}^1 3p^3]_2 3d^1)3/2\rangle$	34.8	216.222	1.399	0.662	−0.730	0.083	0.0420
19	$\|([3\bar{p}^1 3p^3]_2 4s^1)3/2\rangle$	40.6	216.149	7.930	0.381	0.150	0.460	0.0642
20	$\|([3\bar{p}^1 3p^3]_2 4s^1)5/2\rangle$	57.0	216.140	8.631	−0.025	−0.542	−0.320	−0.0507
21	$\|([3\bar{p}^2 3p^2]_2 3d^1)7/2\rangle$	33.2	216.055	0.065	−0.202	−0.175	0.525	0
22	$\|([3\bar{p}^1 3p^3]_1 3d^1)5/2\rangle$	39.1	215.934	16.916	−0.129	−0.291	−0.466	−0.0074
23	$\|([3\bar{p}^2 3p^2]_2 3d^1)3/2\rangle$	20.9	215.655	0.297	0.679	0.145	0.093	−0.0660
24	$\|([3\bar{p}^1 3p^3]_2 3d^1)5/2\rangle$	44.3	215.538	0.395	−0.028	−0.538	−0.323	−0.0491
25	$\|([3\bar{p}^1 3p^3]_2 3\bar{d}^1)7/2\rangle$	68.1	215.252	1.560	−0.202	−0.175	0.525	0
26	$\|([3\bar{p}^1 3p^3]_2 3d^1)9/2\rangle$	71.4	215.192	–	–	–	–	–
27	$\|([3\bar{p}^1 3p^3]_2 3\bar{d}^1)5/2\rangle$	44.2	213.977	6.192	0.068	−0.678	−0.222	−0.0736
28	$\|([3\bar{p}^1 3p^3]_2 3d^1)7/2\rangle$	71.0	213.950	0.430	−0.202	−0.175	0.525	0
29	$\|([3\bar{p}^1 3p^3]_2 3d^1)1/2\rangle$	31.5	213.830	0.059	−0.707	0.408	0.817	0
30	$\|([3\bar{p}^2 3p^2]_0 4s^1)1/2\rangle$	47.9	212.773	0.016	−0.707	0.408	0.817	0
31	$\|([3\bar{p}^2 3p^2]_0 3\bar{d}^1)3/2\rangle$	45.0	211.823	10.781	0.164	0.620	0.689	0.0453
32	$\|([3\bar{p}^0 3p^4]_0 3d^1)5/2\rangle$	27.6	211.767	0.321	0.000	−0.588	−0.290	−0.0559
33	$\|([3\bar{p}^2 3p^2]_2 3d^1)3/2\rangle$	45.0	211.064	0.411	0.212	−0.753	0.229	−0.0144
34	$\|([3\bar{p}^1 3p^3]_2 3d^1)1/2\rangle$	52.4	211.013	8.111	−0.707	0.408	0.817	0
35	$\|([3\bar{p}^2 3p^2]_0 3d^1)5/2\rangle$	40.2	210.198	0.036	0.053	−0.664	−0.235	−0.0685
36	$\|([3\bar{p}^0 3p^4]_0 3\bar{d}^1)3/2\rangle$	39.2	210.025	12.013	0.676	−0.972	−0.064	0.0031

hard to resolve. Thus, it cannot be stated whether the $J_f = 7/2$ or $9/2$ state has been observed. On the other hand, our numerical 36 CSF-CI RDWA approach has not been able to generate the $J_f = 9/2$ final state due to internal selection rules which are suppressing the emission of an $\varepsilon f_{7/2}$ partial wave for the considered transition (see [8] and the discussion above). These two findings allows for an interesting hypothesis. Taking the assignment by Mursu *et al* [11], the particular state under discussion would originate from a three-body interaction. In the usual picture of multi-step two-body interaction, such a final state would require, first, the generation of the $^2G_{7/2}$ state by Auger decay and, subsequently, a shake-up of the Rydberg $3d_{3/2}$ into the $3d_{5/2}$ electron. Such an explanation is however unlikely to happen and overexceeds the

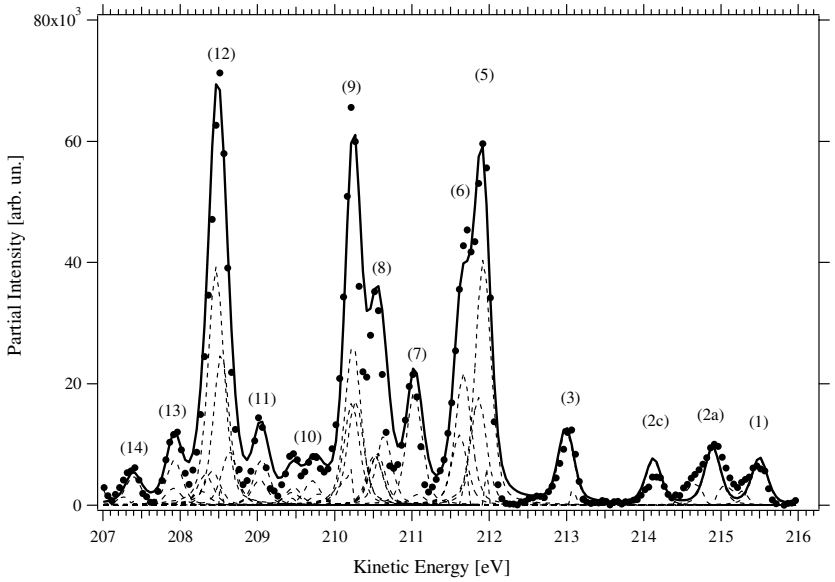

Figure 2. Ar $2p_{1/2}^{-1}$ 3d Auger decay, spin averaged. Circles: experimental, full line: manifold, dashed lines: manifold components (see the text for details).

interpretation of the Auger decay as caused by two-body interaction. Eventually, this leaves us with the possibility of at least qualitatively explaining line 2c by an interaction between the two electrons involved in the Auger decay and the shaking Rydberg electron, resulting in a simultaneous three-electron recombination in the final state. However, neither the resolution of our experiment nor the line intensity is good enough to prove the line designation of the former experiment. Hence, better resolved measurements are necessary to corroborate this interesting aspect.

For a more quantitative comparison, we used a least-squares fit method, where Gaussian functions were used for the manifold components. We forced the relative energy and the relative intensity of the components of the same manifold to be equal to the values by Mursu *et al* [11] whereas we allowed the fitting procedure to adjust the position of the different manifolds. The width of the Gaussian functions was estimated from the few peaks consisting of one or almost one component only, and it was fixed in the fitting procedure. Finally, we further assumed that all the components of the same manifold have similar anisotropy parameters and simply rescaled each manifold's overall intensity to fit our experimental data. The last approximation, though not strictly correct [12], does not seem to introduce too much error. The results are the dashed and continuous curves in figure 2.

Figures 3 and 4 depict the spin-resolved spectra for the TSP and DSP, respectively. Because of the complex structure of the manifolds, we did not try to separate their components in the spin-resolved experimental spectra nor did we fit each manifold with an analytical function. Rather, we took the manifold areas and used them to obtain the spin polarization, assuming that the peak broadening due to finite instrumental resolution does not significantly contribute to the overall area of the manifold. The results are reported in columns 4 and 5 of table 3. For the sign of the polarization, we are adopting the same notation as our previous paper [8], where a positive spin polarization indicates that the electron is emitted preferentially with the spin parallel, rather than anti-parallel, to the photon propagation direction. The errors in table 3 account for both the statistical error (evaluated from the manifold areas) and the

Table 3. Peaks assignment and their measured spin polarization.

Peak	Final state	Binding energy (eV)	Ar $2p_{1/2}3d$ transferred polarization	Ar $2p_{1/2}3d$ dynamic polarization	Ar $2p_{1/2}4s$ transferred polarization	Ar $2p_{1/2}4s$ dynamic polarization
1	$3p^4(^3P)3d\ ^4F_{3/2,5/2}$	33.50	−0.14 (0.2)	+0.2 (0.3)	−0.05 (0.06)	+0.03 (0.03)
2a–b	$3p^4(^3P)3d\ ^4P$	34.05	+0.25 (0.15)	−0.1 (0.2)	−0.36 (0.06)	+0.03 (0.03)
2c	$3p^4(^1D)3d\ ^2G_{7/2,9/2}$	34.88	+0.13 (0.25)	+0.7 (0.4)	–	–
3	$3p^4(^1D)3d\ ^2F_{5/2}$	36.00	+0.33 (0.2)	−0.15 (0.2)	–	–
4	$3p^4(^1S)4s\ ^2S_{1/2}$	36.50	–	–	−0.8 (0.2)	−0.06 (0.07)
5	$3p^4(^1D)3d\ ^2D_{5/2}$	37.13	+0.1 (0.05)	+0.06 (0.09)	−0.36 (0.2)	−0.35 (0.1)
	$3p^4(^1D)3d\ ^2D_{3/2}$	37.19				
6	$3p^4(^1D)3d\ ^2P_{3/2}$	37.38				
	$3p^4(^1D)3d\ ^2P_{1/2}$	37.44				
7	$3p^4(^1S)3d\ ^2D_{5/2}$	38.03	+0.3 (0.1)	−0.03 (0.2)	–	–
	$3p^4(^1S)3d\ ^2D_{3/2}$	38.07				
8	$3p^4(^3P)5s\ ^2P_{1/2}$	38.46	+0.01 (0.05)	+0.11 (0.09)	+0.11 (0.2)	+0.19 (0.13)
	$3p^4(^3P)4d\ ^4D_{5/2}$	38.55				
	$3p^4(^3P)4d\ ^4D_{3/2}$	38.57				
9	$3p^4(^1D)3d\ ^2S_{1/2}$	38.59				
	$3p^4(^3P)4d\ ^4F_{5/2}$	38.83				
	$3p^4(^3P)4d\ ^4F_{3/2}$	38.86				
	$3p^4(^3P)4d\ ^4P_{3/2}$	38.88				
10	–	39.24	−0.18 (0.15)	+0.05 (0.2)	–	–
	$3p^4(^3P)4d\ ^2P_{1/2,3/2}$	39.31				
	$3p^4(^3P)4d\ ^2D_{5/2}$	39.63				
	$3p^4(^3P)4d\ ^2D_{3/2}$	39.65				
11	$3p^4(^1D)5s\ ^2D_{5/2}$	40.04	−0.3 (0.2)	+0.45 (0.2)	+0.45 (0.4)	+0.56 (0.3)
	$3p^4(^3P)4f\ J = 3/2$	40.07				
12	$3p^4(^3P)6s\ ^4P_{5/2}$	40.41	+0.18 (0.07)	+0.05 (0.1)	–	–
	$3p^4(^1D)4d\ ^2D_{5/2}$	40.52				
	$3p^4(^1D)4d\ ^2F_{5/2}$	40.59				
	$3p^4(^3P)6s\ ^2P_{1/2}$	40.63				
	$3p^4(^3P)5d\ ^4P_{3/2}$	40.72				
	$3p^4(^3P)5d\ ^4P_{5/2}$	40.78				
13	$3p^4(^3P)5d\ ^2D_{3/2}$	41.10	+0.21 (0.2)	+0.4 (0.2)	–	–
	$3p^4(^3P)5d\ ^2P_{1/2}$	41.12				
14	$3p^4(^3P)6d\ ^4P_{1/2}$	41.61	−0.12 (0.2)	0 (0.02)	–	–

uncertainty in the Sherman function. Also, we performed the same analysis for the newly collected spectra of the Auger decay of the Ar $2p_{1/2}^{-1}4s$ state and reported the results in columns 6 and 7 of table 3. The latter show reasonable agreement with our previous measurement for peaks 1–4, they have larger errors due to a lower statistic of the new measurements. In general, the TSP is stronger for the decay of the $2p_{1/2}^{-1}4s$ than $2p_{1/2}^{-1}3d$. In contrast, the $2p_{1/2}^{-1}3d$ state shows significant amount of the DSP for peaks 2c, 11 and 13. The measured large DSP of ∼70% for line 2c leaves us with more ambiguities. As can be extracted from table 2, our 36 CSF-CI RDWA is able to generate the line, though, with a vanishing DSP,

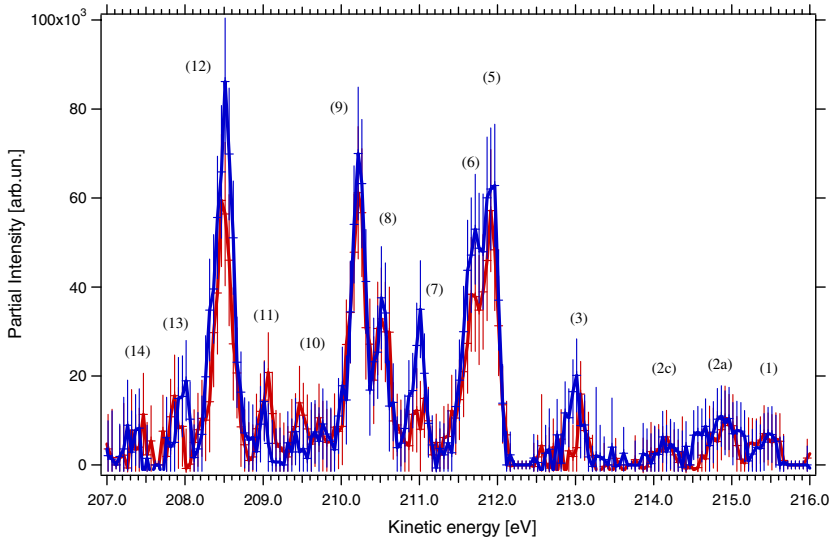

Figure 3. Spin-resolved spectrum of Ar $2p_{1/2}3d$ Auger decay as measured with circularly polarized light. Blue: spin parallel, red: spin anti-parallel, to photon propagation direction.

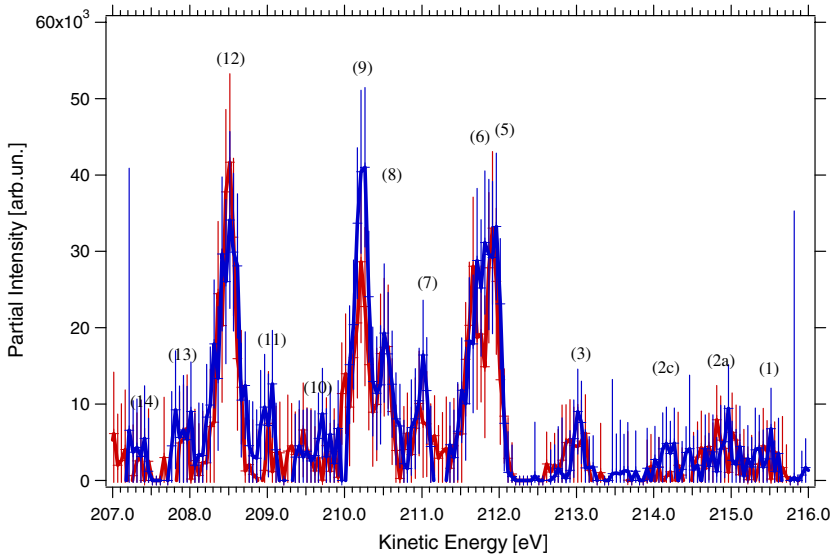

Figure 4. Same as figure 3 for linearly polarized light.

which might be interpreted as in favour of the discussed hypothesis (see above). Peak 12 in figure 4 suggests that its components have strong DSP, though the total polarization vanishes when the manifold is not resolved. Also, peaks 11 and the unresolved 8–9 show similar values of the DSP in the $2p_{1/2}^{-1}$ 4s and $2p_{1/2}^{-1}$ 3d decay.

The results of the 36 CSF-CI calculations for the $2p_{1/2}^{-1}$ 3d state are compared to the TSP and DSP we measured in the 33.5–37 eV binding energy range in figures 5 and 6, respectively,

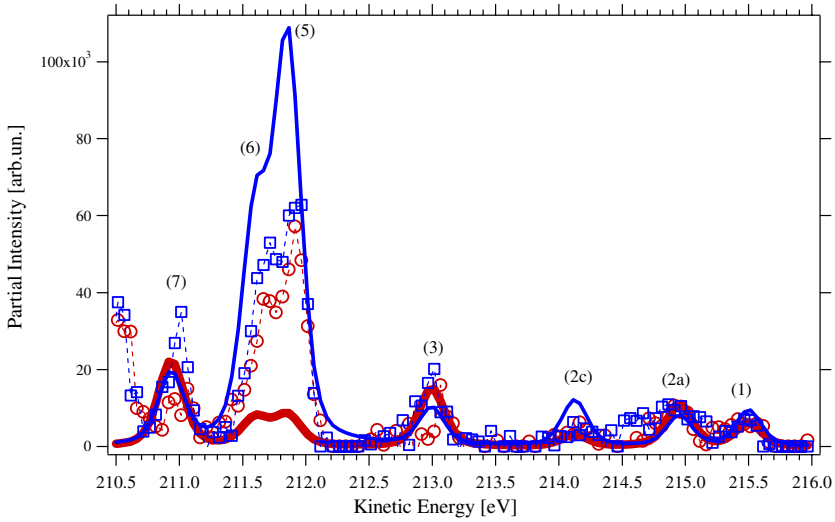

Figure 5. TSP of Ar $2p_{1/2}3d$ Auger decay, comparison with 36 CFS calculations. Experimental: (□) spin parallel, (○) anti-parallel. Calculations: full blue line, parallel; full red line, anti-parallel. Dashed lines are added to experimental data to guide the eye.

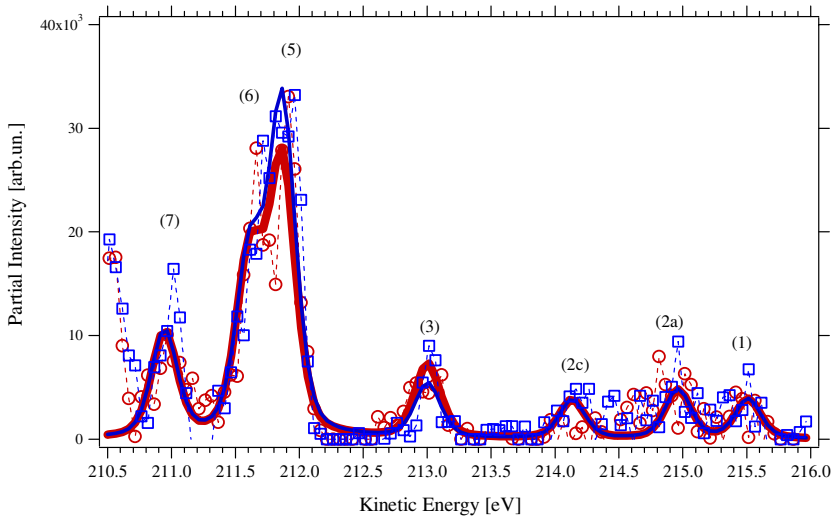

Figure 6. Same as figure 5 for the DSP.

and in table 4. The relative intensities, positions and widths of the peaks, as obtained by the fitting of the spin-unresolved spectrum using the procedure described above and depicted in figure 2, were used. These were combined with the calculated spin polarization reported in columns 6 and 8 of table 4, resulting in the full bold lines depicted in figures 5 and 6. The calculations correctly reproduce the DSP, with the only exception of peak 2c. In contrast, they strongly overestimate the TSP of peak 5, and they find the wrong sign of the polarization of peaks 3 and 7. The remaining agreement between calculation and theory would suggest that for the $2p_{1/2}^{-1}$ 3d state it is the TSD, rather than the DSP as we showed for the $2p_{1/2}^{-1}$ 4s

Table 4. Measured and calculated spin polarization for the Ar $2p_{1/2}$ 3d Auger decay.

Peak	Final state	State number[a]	Binding energy (eV)	Measured transferred polarization	Calculated transferred polarization	Measured dynamic polarization	Calculated dynamic polarization
1	$3p^4(^3P)3d\ ^4F_{3/2,5/2}$	10–13	33.50	−0.14 (0.2)	+0.21	+0.2 (0.3)	≈0
2a–b	$3p^4(^3P)3d\ ^4P$	14–24	34.05	+0.25 (0.15)	−0.17	−0.1 (0.2)	≈0
2c	$3p^4(^1D)3d\ ^2G_{7/2,9/2}$	25, 26	34.88	+0.13 (0.25)	+0.60	+0.7 (0.4)	0
3	$3p^4(^1D)3d\ ^2F_{5/2}$	27–29	36.00	+0.33 (0.2)	−0.21	−0.15 (0.2)	−0.15
4	$3p^4(^1S)4s\ ^2S_{1/2}$	30	36.50	–	+0.80[b]	–	0
5	$3p^4(^1D)3d\ ^2D_{5/2}$	31–32	37.13	+0.1 (0.05)	+0.86 (peak 5)	+0.06 (0.09)	+0.10 (peak 5)
	$3p^4(^1D)3d\ ^2D_{3/2}$		37.19				
6	$3p^4(^1D)3d\ ^2P_{3/2}$	33–34	37.38		+0.78 (peak 6)		≈0 (peak 6)
	$3p^4(^1D)3d\ ^2P_{1/2}$		37.44				
7	$3p^4(^1S)3d\ ^2D_{5/2}$	35–36	38.03	+0.3 (0.1)	−0.10	−0.03 (0.2)	+0.01
	$3p^4(^1S)3d\ ^2D_{3/2}$		38.07				

[a] According to our numerical 36 jj-coupled CSF calculation, as labelled in the first column of tables 1 and 2.
[b] Calculations state a high TSP but a vanishing intensity for this line, which in fact could not be measured experimentally.

[8], which is more sensitive to the calculation details. To test this hypothesis, an extended approach, including a larger basis set than the 36 CSF-CI, should be tempted, which is however beyond the scope of this paper. Such an extended-basis calculation is also expected to give more accurate results for the relative line intensities, which are not well reproduced by the 36 CSF-CI calculation, in particular the large intensities of peaks 5–7 as compared to peaks 1–3. An attempt into that direction has been recently performed by Fritzsche *et al* [28].

6. Conclusions

We showed that the DSP already observed in the Auger decay of the $2p_{1/2}^{-1}$ 4s is also observable, even partly stronger, in the Auger decay of the $2p_{1/2}^{-1}$ 3d state at medium energy resolution. For the latter state, an interpretation of the DSP as configuration interaction induced effect in the final ionic state leads to partial agreement with our relativistic distorted wave approximation utilizing a 36 configuration state functions basis set. We found evidence for a large DSP of an Auger line where the particular problems arising from a previous identification of the specific line have been discussed and a hypothetical, qualitative interpretation has been given. Our results show that the achievements in spin polarization calculations over the last years are very high compared to former calculations, but still need further improvement in the future. This, on the other hand, shows the need for angle- and spin-resolved high-resolution experiments in order to allow for a more detailed comparison.

Acknowledgments

Experimental work at the ALS was funded by the US DOE, Office of Science, BES, Divisions of Chemical, Biosciences, and Geophysical Sciences. We are grateful to J Bozek and A Young for their help in the measurements at the beamline.

References

[1] Kabachnik N M, Sazhina I P, Lee I S and Lee O V 1988 *J. Phys. B: At. Mol. Opt. Phys.* **21** 3695
[2] Lohmann B, Hergenhahn U and Kabachnik N M 1993 *J. Phys. B: At. Mol. Opt. Phys.* **26** 3327
[3] Snell G, Drescher M, Müller N, Heinzmann U, Hergenhahn U, Viefhaus J, Heiser F, Becker U and Brookes N B 1996 *Phys. Rev. Lett.* **76** 3923
[4] Snell G, Langer B, Drescher M, Müller N, Zimmermann B, Hergenhahn U, Viefhaus J, Heinzmann U and Becker U 1999 *Phys. Rev. Lett.* **82** 2480
[5] Müller N *et al* 1995 *J. Electron Spectrosc. Relat. Phenom.* **72** 187
[6] Hergenhahn U, Snell G, Drescher M, Schmidtke B, Müller N, Heinzmann U, Wiedenhöft M and Becker U 1999 *Phys. Rev. Lett.* **82** 5020
[7] Lohmann B 1999 *J. Phys. B: At. Mol. Opt. Phys.* **32** L643
[8] Lohmann B, Langer B, Snell G, Kleiman U, Canton S, Martins M, Becker U and Berrah N 2005 *Phys. Rev.* A **71** 020701
[9] Klar H 1980 *J. Phys. B: At. Mol. Phys.* **13** 4741
[10] Kabachnik N M 1981 *J. Phys. B: At. Mol. Phys.* **14** L337
[11] Mursu J, Aksela H, Sairanen O-P, Kivimaki A, Nommiste E, Ausmees A, Svensson S and Aksela S 1996 *J. Phys. B: At. Mol. Opt. Phys.* **29** 4387
[12] Farhat A, Humphrey M, Langer B, Berrah N, Bozek J D and Cubaynes D 1997 *Phys. Rev.* A **56** 501
[13] Aksela H, Aksela S, Pulkkinen H, Bancroft G M and Tan K H 1988 *Phys. Rev.* A **37** 1798
[14] Meyer M, Raven E V, Sonntag B and Hansen J E 1991 *Phys. Rev.* A **43** 177
[15] Meyer M, von Raven E, Richter M, Sonntag B and Hansen J E 1990 *J. Electron Spectrosc. Relat. Phenom.* **51** 407
[16] Langer B, Berrah N, Farhat A, Humphrey M, Cubaynes D, Menzel A and Becker U 1997 *J. Phys. B: At. Mol. Opt. Phys.* **30** 4255
[17] Mehlhorn W 1990 *X-Ray and Inner Shell Processes* ed T A Carlson *et al* (New York: AIP) p 465 (*AIP Conf. Proc.* vol 215)
[18] Kleiman U, Lohmann B and Blum K 1999 *J. Phys. B: At. Mol. Opt. Phys.* **32** L219
[19] Kronast W, Huster R and Mehlhorn W 1986 *Z. Phys.* D **2** 285
[20] Snell G, Langer B, Young A T and Berrah N 2002 *Phys. Rev.* A **66** 022701
[21] Burnett G C, Monroe T J and Dunning F B 1994 *Rev. Sci. Instrum.* **65** 1893
[22] Snell G, Viefhaus J, Dunning F B and Berrah N 2000 *Rev. Sci. Instrum.* **71** 2608
[23] Grant I P, McKenzie B, Norrington P, Mayers D and Pyper N 1980 *Comput. Phys. Commun.* **21** 207
[24] Lohmann B 1999 *Aust. J. Phys.* **52** 397
[25] Lohmann B and Kleiman U 2001 *Many Particle Spectroscopy of Atoms Molecules, and Surfaces* ed J Berakdar and J Kirschner (New York: Kluwer/Plenum) p 173
[26] Lohmann B 1998 *Habilitation Thesis* University of Münster
[27] Grant I P 1970 *Adv. Phys.* **19** 747
[28] Fritzsche S, Nikkinen J, Huttula S-M, Aksela H, Huttula M and Aksela S 2007 *Phys. Rev.* A **75** 012501
[29] Becker U and Shirley D A 1996 *VUV and Soft X-Ray Photoionization* (New York: Plenum) p 146 and references therein
[30] de Gouw J A, van Eck J, Peters A C, van der Weg J and Heideman H G M 1995 *J. Phys. B: At. Mol. Opt. Phys.* **28** 2127
[31] Chen M H 1993 *Phys. Rev.* A **47** 3733
[32] Lohmann B, Langer B, Snell G, Kleiman U, Canton S, Martins M, Becker U and Berrah N 2003 *Correlation and Polarization in Photonic Electronic and Atomic Collisions* ed G F Hanne *et al* (Melville, NY: AIP) p 133 (*AIP Conf. Proc.* vol 697)